

Fundamental parameters for dEB SB2 binary system J064726.39+223431.6. A new challenge for stellar evolution models.

Mikhail Kovalev,^{1,2,3,4★} Song Wang,⁵ Xuefei Chen^{1,2,6} and Zhanwen Han^{1,2,6}

¹Yunnan Observatories, China Academy of Sciences, Kunming 650216, China

²Key Laboratory for the Structure and Evolution of Celestial Objects, Chinese Academy of Sciences, Kunming 650011, China

³Sternberg Astronomical Institute of M. V. Lomonosov Moscow State University, Leninskie Gory, Moscow 119991, Russia

⁴Max Planck Institute for Astronomy, D-69117 Heidelberg, Germany

⁵Key Laboratory of Optical Astronomy, National Astronomical Observatories, Chinese Academy of Sciences, Beijing 100101, China

⁶Center for Astronomical Mega-Science, Chinese Academy of Sciences, 20A Datun Road, Chaoyang District, Beijing 100012, China

Accepted XXX. Received YYY; in original form 26-09-2022

ABSTRACT

We present a study of eclipsing binary J064726.39+223431.6 using spectra from the LAMOST-MRS and TESS photometry. We use full-spectrum fitting to derive radial velocities and spectral parameters: $T_{\text{eff},A,B} = 6177, 5820$ K, $V \sin i_{A,B} = 59, 50$ km s^{−1} and $[\text{Fe}/\text{H}]_{A,B} = -0.19$ dex. The orbital solution and light curve analysis suggest that it is a close pair of fast rotating stars on circular orbit. We measure their masses to be $M_{A,B} = 1.307 \pm 0.007, 1.129 \pm 0.005 M_{\odot}$ and their radii to be $R_{A,B} = 1.405 \pm 0.052, 1.219 \pm 0.060 R_{\odot}$ resulting in surface gravities of $\log(g)_{A,B} = 4.259 \pm 0.033, 4.319 \pm 0.042$ (cgs). Theoretical models cannot match all of these properties, predicting significantly higher T_{eff} for a given metallicity. Derived age of the system 1.56 Gyr indicates that both components are younger than Sun. J064726.39+223431.6 is a good candidate for high-resolution spectroscopic analyses.

Key words: stars : fundamental parameters – binaries : spectroscopic – stars individual: J064726.39+223431.6

1 INTRODUCTION

Binary stellar systems are very important objects for astronomy, since they allow us to learn more than from single stars. For example observations of the periodic eclipses and changes in line-of-sight velocities (RV) to directly measure sizes and masses of the stellar components, if orbital inclination is high enough. Such measurements are very useful to constrain theoretical models of stellar evolution.

Many double-lined spectroscopic binaries (SB2) were identified in Kovalev (2022) based on LAMOST (Large Sky Area Multi-Object fiber Spectroscopic Telescope) medium resolution spectra (Liu et al. 2020) and we selected one previously known detached eclipsing binary (dEB) star with large RV semi-amplitude based on Wang et al. (2021) to estimate physical parameters for both components in this system. Variable Star index (Watson et al. 2006) database contains it as Algol type variable under ID: 167003 with observations available in ZTF (Chen et al. 2020) and ASAS-SN V (Jayasinghe et al. 2018). It is included in the recent Gaia DR3 (Gaia Collaboration et al. 2022) as 3378682653860701568 with $G = 13.416055 \pm 0.002923$ mag and parallax $\varpi = 0.8915 \pm 0.0177$ mas. This star is included in the TESS input catalogue (TIC Stassun

et al. 2019) as TIC57046871, with no light curve (LC) data publicly available on MAST¹ portal yet.

In this paper we use LAMOST-MRS spectra and additional photometrical data to measure physical parameters for both stars in this system. The paper is organised as follows: in Sections 2,3 we describe the observations and methods. Section 4 presents our results. In Section 5 we discuss the results in context of binary system evolution. In Section 6 we summarise the paper and draw conclusions.

2 OBSERVATIONS

2.1 Spectra

LAMOST (Large Sky Area Multi-Object fiber Spectroscopic Telescope; also known as Guo Shou Jing telescope) is a 4-meter quasi-meridian reflective Schmidt telescope with 4000 fibers installed on its 5-degree-FoV focal plane. These configurations allow it to observe spectra for at most 4000 celestial objects simultaneously (Cui et al. (2012); Zhao et al. (2012)). All available spectra were downloaded from www.lamost.org under the designa-

★ E-mail: mikhail.kovalev@ynao.ac.cn

¹ <https://mast.stsci.edu/portal/Mashup/Clients/Mast/Portal.html>

tion J064726.39+223431.7. We use the spectra taken at a resolving power of $R = \lambda/\Delta\lambda \sim 7500$. Each spectrum is divided on two arms: blue from 4950 Å to 5350 Å and red from 6300 Å to 6800 Å. We convert the heliocentric wavelength scale in the observed spectra from vacuum to air using PyAstronomy (Czesla et al. 2019). Observations are carried out from 2019-11-19 till 2021-02-19, covering 16 nights with time base of 480 days. As period is short ($P = 1.217$ d ~ 29 hrs) we analysed spectra taken during individual 20 minutes exposures, unlike Kovalev et al. (2022) where spectra stacked for the whole night were used. We discarded all spectra taken on three nights with MJD=58829, 59216, 59249 d as very noisy. In total we have 72 spectra, where the average signal-to-noise ratio (S/N) of a spectrum ranges from 16 to 54 pix^{-1} with the majority of the spectra have S/N around 40 pix^{-1} .

2.2 Photometry

We download publicly available ZTF light curves (LC)². These LC contain 1444 datapoints in *r* band and 370 datapoints in *g* bands and cover timebase 1240 d and 1125 d respectively. We also download LC in *V* band from ASSAS-SN portal³. It contains only 183 datapoints and covers timebase 1212 d. After phase-folding of these LC with the period we found that only ZTF LC from *r* band has good coverage of eclipses, therefore we use only it in the further analysis.

The Transiting Exoplanet Survey Satellite (TESS Ricker et al. 2015) mission observed this star in two sectors 44 and 45, which covers ~ 27 days each. The LCs are not available on MAST portal yet, therefore we use eleanor (Feinstein et al. 2019; Brasseur et al. 2019) to extract the LC datasets. We use default settings and clip the edges of the LC, as they have some processing artifacts, see Figure 1. After the clipping LCs contain 2953 and 3160 datapoints for sectors 44 and 45 respectively and have relative (non-calibrated) stellar magnitudes. The background subtraction is not optimal for these datasets, therefore we analyse them separately.

3 METHODS

3.1 Spectral fitting

Our spectroscopic analysis includes two consecutive stages:

(i) analysis of individual observations by binary and single-star spectral models, where we normalise the spectra and make rough estimation of the spectral parameters, see brief description in Section 3.1.1.

(ii) simultaneous fitting of multiple-epochs with a binary spectral model, using constraints from binary dynamics and values from the previous stage as an input, see Section 3.1.2.

LAMOST-MRS implementation of this method was first presented in Kovalev et al. (2022).

3.1.1 Individual spectra.

Single-star spectral model is described in Appendix A. The normalised binary model spectrum is generated as a sum of the two Doppler-shifted normalised single-star model spectra $f_{\lambda,i}$ scaled

according to the difference in luminosity, which is a function of the T_{eff} and stellar size. We assume both components to be spherical and use following equation:

$$f_{\lambda,\text{binary}} = \frac{f_{\lambda,2} + k_{\lambda} f_{\lambda,1}}{1 + k_{\lambda}}, \quad k_{\lambda} = \frac{B_{\lambda}(T_{\text{eff},1}) M_1}{B_{\lambda}(T_{\text{eff},2}) M_2} 10^{\log(g)_2 - \log(g)_1} \quad (1)$$

where k_{λ} is the luminosity ratio per wavelength unit, B_{λ} is the black-body radiation (Planck function), T_{eff} is the effective temperature, $\log(g)$ is the surface gravity and M is the mass. Throughout the paper we always assume the primary star to be brighter.

The binary model spectrum is later multiplied by the normalisation function, which is a linear combination of the first four Chebyshev polynomials (similar to Kovalev et al. 2019), defined separately for blue and red arms of the spectrum. The resulting spectrum is compared with observed one using `scipy.optimize.curve_fit` function, which provides optimal spectral parameters, radial velocities (RV) of each component plus mass ratio and two sets of four coefficients of Chebyshev polynomials. We keep metallicity equal for both components. In total we have 18 free parameters for a binary fit. We estimate goodness of the fit parameter by reduced χ^2 :

$$\chi^2 = \frac{1}{N-18} \sum [(f_{\lambda,\text{observed}} - f_{\lambda,\text{model}}) / \sigma_{\lambda}]^2 \quad (2)$$

where N is a number of wavelength points in the observed spectrum. To explore whole parameter space and to avoid local minima we run optimisation six times with different initial parameters of the optimiser. We select the solution with minimal χ^2 as a final result.

Additionally, every spectrum is analysed by a single star model, which is identical to a binary model when both components have all equal parameters, so we fit only for 13 free parameters. Using this single star solution we compute the difference in reduced χ^2 between two solutions and the improvement factor, computed using Equation 3 similar to El-Badry et al. (2018). This improvement factor estimates the absolute value difference between two fits and weights it by difference between two solutions.

$$f_{\text{imp}} = \frac{\sum [(|f_{\lambda,\text{single}} - f_{\lambda}| - |f_{\lambda,\text{binary}} - f_{\lambda}|) / \sigma_{\lambda}]}{\sum [|f_{\lambda,\text{single}} - f_{\lambda,\text{binary}}| / \sigma_{\lambda}]}, \quad (3)$$

where f_{λ} and σ_{λ} are the observed flux and corresponding uncertainty, $f_{\lambda,\text{single}}$ and $f_{\lambda,\text{binary}}$ are the best-fit single-star and binary model spectra, and the sum is over all wavelength pixels.

3.1.2 Multiple-epochs fitting.

We explore results from the fitting of the individual epochs and find that result's quality clearly depends on separation of RVs. Clear double-lined spectra show that spectral lines are significantly broadened ($V \sin i \sim 60 \text{ km s}^{-1}$), thus at phases near the conjunctions our fitting algorithm often cannot reliably separate primary/secondary contributions. Fortunately we can automatically separate good results with clear double-lines using f_{imp} . Thus we decided to use only five individual spectra with highest f_{imp} in multi-epoch fitting.

If two components in our binary system are gravitationally bound, their radial velocities should agree with the following equation:

$$RV_A = \gamma_{\text{dyn}}(1 + q_{\text{dyn}}) - q_{\text{dyn}}RV_B, \quad (4)$$

where $q_{\text{dyn}} = M_B/M_A$ - mass ratio of binary components and γ_{dyn}

² https://irsa.ipac.caltech.edu/cgi-bin/ZTF/nph_light_curves

³ <https://asas-sn.osu.edu/variables/AP24824756>

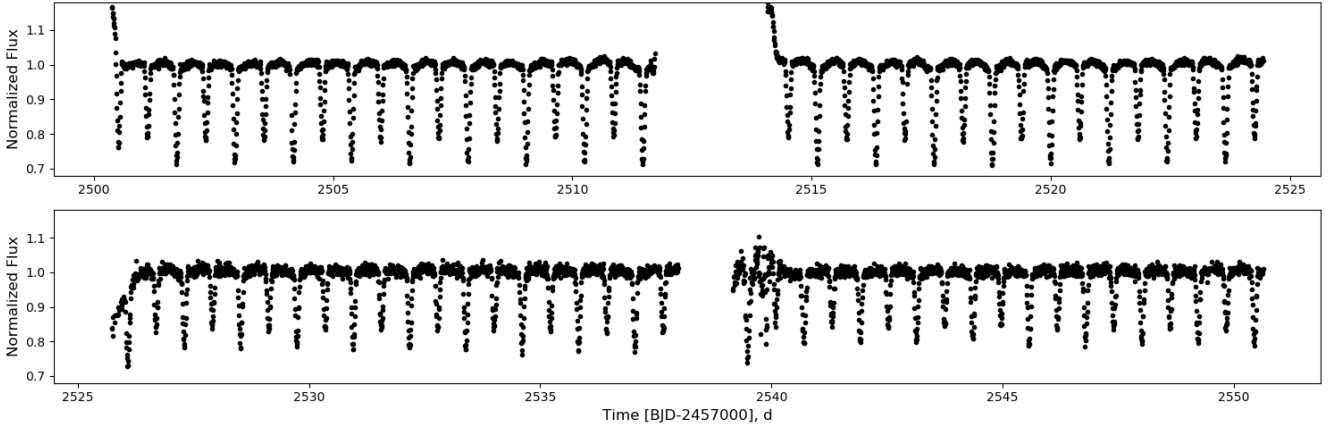


Figure 1. Light curves extracted by *eleanor* from TESS sectors 44 (top) and 45 (bottom).

- systemic velocity. Using this equation we can directly measure the systemic velocity and mass ratio.

To reduce the number of free parameters in multiple-epochs fitting we use only RV_A and computed RV_B using Equation 4. The same value of mass ratio is used in Equation 1. Unlike the previous stage we fit $[Fe/H]$ for both components. In total we fit for 15 free parameters. We fit five previously normalised individual epoch's spectra with maximal improvement factor, using their binary spectral parameters values for initialisation. We select the solution with minimal χ^2 as a final result.

3.1.3 Typical errors estimation

We estimate typical errors of the multiple-epochs fitting by testing it's performance on the dataset of synthetic binaries. We generated 3000 mock binaries using uniformly distributed mass-ratios from 0.7 to 1.0, T_{eff} from 4600 to 8400 K, $\log(g)$ from 2.6 to 4.6 (cgs) and $V \sin i$ from 1 to 100 km s^{-1} . Metallicity was set to $[Fe/H] = 0.0$ dex in both components. For each star, we computed 5 mock binary spectra using radial velocities computed for circular orbits with the semiamplitude of the primary component 20 km s^{-1} at randomly chosen phases. These models were degraded by Gaussian noise according to $S/N = 100 \text{ pix}^{-1}$. We performed exactly the same analysis as for the observations on this simulated dataset. We checked how well the mass ratio and the spectral parameters of the primary and secondary components can be recovered by calculating the average and standard deviation of the residuals. For the primary components we have $\Delta T_{\text{eff}} = 95 \pm 239 \text{ K}$, $\Delta \log(g) = 0.07 \pm 0.14$ cgs units, $\Delta V \sin i = -1 \pm 12 \text{ km s}^{-1}$ and $\Delta [Fe/H] = -0.02 \pm 0.08$ dex. For the secondary components we have $\Delta T_{\text{eff}} = 35 \pm 364 \text{ K}$, $\Delta \log(g) = 0.05 \pm 0.21$ cgs units, $\Delta V \sin i = -3 \pm 21 \text{ km s}^{-1}$ and $\Delta [Fe/H] = 0.04 \pm 0.18$ dex. The mass ratio recovery has $\Delta q = 0.05 \pm 0.15$.

3.2 Orbital fitting

To get orbital solution we select 55 RVs of the primary component separated by at least 60 km s^{-1} from the systemic velocity γ . RVs close to γ can be affected by the Rossiter-McLaughlin (RM) effect (Rossiter 1924; McLaughlin 1924), as several spectra were possibly taken during eclipses, thus we don't use them in orbital fitting. We collect all RV measurements in Table 1

In the next step, selected RV_A are used to fit circular orbits using generalised Lomb-Scargle periodogram (GLS) code by Zechmeister & Kürster (2009) :

$$RV_A(t) = \gamma - K_A \sin\left(\frac{2\pi}{P}(t - t_0)\right), \quad (5)$$

where γ - systemic velocity, P - period, t_0 - conjunction time, K - radial velocity semiamplitude.

We also fit to a Keplerian orbit and find that eccentricity is equal to zero, so a circular orbit is a valid assumption.

3.3 Light curve fitting

We used JKTEBOP code (version 40)⁴ by Southworth (2013) to simultaneously fit the LC and RV timeseries. We used only ZTF r band and TESS datasets, because of their better coverage of the eclipses. Unlike GLS, JKTEBOP allows us to fit RVs measured for both components. Our fitting was initialised using P, t_0, γ values from the GLS fit. We used tables of the limb/gravity darkening coefficients from Claret & Bloemen (2011); Claret (2017) and linearly interpolated them for spectral parameters from multiple-epochs fits. We used four-parameter limb darkening coefficients c_i , $i = 1, 4$. We took into account useful comment by Torres (2021) on the usage of gravity darkening coefficients in JKTEBOP.

The systemic velocity was fitted for both binary components. Additionally we fit for a "third" light contribution L_3 and the nuisance parameter the out-of-eclipse magnitude S_0 for all three datasets. In total we fit for 16 parameters: J the central surface brightness ratio, $(R_A + R_B)/a$ the ratio of the sum of stellar radii to the semimajor axis, R_B/R_A the ratio of the radii, i the inclination, $e \cos \omega$, $e \sin \omega$ the eccentricity multiplied by the cosine and sine of the periastron longitude, reflected light $A_{A,B}$, P the period, t_0 , semiamplitudes and systemic velocities $K_{A,B}$, $\gamma_{A,B}$, L_3 and S_0 . We use integration ring size 5° for the ZTF r and 1° for the TESS LCs.

At first we run JKTEBOP code in the mode "Task 4" to discard outliers larger than three sigma and allow it adjusting observational errors through several iterations until reduced χ^2 will reach unity.

⁴ JKTEBOP is written in FORTRAN77 and the source code is available at <http://www.astro.keele.ac.uk/jkt/codes/jktebop.html>

Table 1. Radial velocity measurements. The asterisk (*) denotes data-points which are not used in analysis with GLS and JKTEBOP. We subtract 2400000.5 days from time values.

time HJD d	multiple-epochs RV _A km s ⁻¹	ind. epoch RV _B , RV _A km s ⁻¹	single RV km s ⁻¹
58806.74		-169.77±2.50, 98.54±2.07	-7.01
58806.76		-159.21±2.72, 103.66±1.71	-1.42
58806.78		-159.98±1.02, 106.50±0.70	-5.79
58806.79		-158.66±1.12, 106.87±0.80	2.57
58806.81		-158.83±0.97, 103.80±0.68	-5.38
58806.82		-155.77±1.06, 103.79±0.72	-7.45
58806.84		-152.48±1.11, 100.31±0.72	-0.87
58806.86		-151.16±1.10, 96.59±0.79	-9.72
58820.77		124.71±0.89, -141.97±0.66	-20.69
58820.78		124.27±0.97, -139.47±0.66	-26.77
58820.79	-140.06±0.57	123.54±0.92, -140.18±0.64	-21.63
58820.80		121.96±1.00, -139.56±0.69	-23.36
58820.81		122.94±1.00, -139.70±0.73	-16.79
58820.82		123.32±0.92, -138.43±0.68	-19.63
58820.83		121.06±1.01, -137.90±0.67	-26.18
58835.74		3.96±1.90, -40.86±2.70*	-12.50
58835.75		24.66±1.34, -45.46±1.58*	-9.52
58835.77		22.22±1.08, -64.15±1.63*	-9.63
58835.78		30.49±0.91, -74.37±1.36*	-10.97
58856.64		-149.11±1.20, 96.22±0.84	0.62
58856.66		-154.25±1.13, 98.60±0.87	-8.63
58856.67		-157.34±1.25, 104.05±0.90	-2.07
58856.69		-157.91±0.99, 105.83±0.71	-12.86
58856.70		-158.98±1.20, 105.49±0.84	-6.12
58856.72		-158.31±1.05, 106.23±0.83	-12.57
58860.67		-27.99±3.65, -9.49±2.36*	-16.65
58860.68		-39.85±3.50, 0.21±2.98*	-21.37
58860.70		-41.39±2.49, 9.52±3.42*	-20.35
58860.72		-43.71±1.84, 25.16±2.84*	-22.23
58883.56	100.76±0.46	-154.79±0.85, 101.26±0.63	-8.13
58883.57		-151.01±0.91, 96.86±0.67	-8.01
58883.59		-145.40±1.23, 93.86±0.88	-8.07
58883.61		-140.24±1.00, 88.86±0.72	-8.89
58883.62		-132.46±0.95, 83.10±0.72	-13.08
58889.54	100.37±0.43	-155.40±0.78, 100.59±0.59	-6.28
58889.55	103.53±0.46	-157.68±0.91, 103.44±0.63	-9.97
58889.57		-158.45±1.17, 106.64±0.86	-3.32
58889.58		-157.72±1.20, 105.39±0.87	-5.89
58889.60		-159.82±1.15, 106.04±0.86	-10.49
58889.62		-157.74±1.38, 104.89±1.03	-7.40
58889.63		-157.47±1.70, 103.59±1.28	-7.53
58919.48		120.69±1.05, -134.31±0.73	-25.05
58919.50		115.05±0.93, -131.58±0.65	-23.05
58919.52		115.08±1.11, -127.50±0.75	-13.90
58919.53		103.32±1.31, -120.86±0.84	-25.18
58919.55		100.36±1.10, -116.91±0.76	-17.02

This removes 24, 17, 13 datapoints from ZTF *r*, TESS 44, 45 LC datasets and keeps all 110 RV datapoints. Then we run JKTEBOP code in the residual permutation (RP) mode (Task 9 - "red" noise) to estimate uncertainties using 1417, 2935 and 3147 residual-shifted fits for ZTF *r* and TESS 44, 45 datasets respectively, similarly to Southworth et al. (2011); Southworth (2013).

Table 1 – continued

HJD d	multiple-epochs RV _A km s ⁻¹	ind. epoch RV _B , RV _A km s ⁻¹	single RV km s ⁻¹
59149.81		42.48±1.03, -67.68±0.75*	-26.09
59149.83		29.63±1.34, -61.11±0.89*	-27.31
59149.84		1.57±1.21, -63.52±1.05*	-25.46
59149.86		24.68±2.57, -39.14±1.14*	-24.76
59149.88		-3.04±2.01, -36.29±1.66*	-21.09
59149.89		-10.16±1.36, -28.63±2.69*	-15.98
59149.91		-5.62±2.65, -25.12±3.82*	-13.35
59180.76		-134.31±1.42, 84.06±1.00	-7.81
59180.78		-130.97±1.68, 78.87±1.14	-15.45
59180.79		-121.85±1.40, 73.23±1.03	-14.22
59180.81		-112.51±1.68, 67.83±1.22	-4.65
59180.82		-97.08±1.62, 57.49±1.27	-14.16
59189.73		-136.89±0.94, 120.61±1.38	-22.00
59189.75		-139.65±1.24, 122.79±1.66	-16.01
59189.77		125.09±1.54, -141.53±1.06	-13.64
59189.78		125.75±1.80, -136.33±1.12	-12.49
59235.59		-121.19±0.94, 71.44±0.65	-9.07
59235.61		-109.18±1.12, 60.83±0.72	-12.97
59235.62		-101.27±1.09, 56.43±0.75	-13.91
59235.64		-89.90±1.06, 47.93±0.71	-14.00
59235.66		-79.47±1.01, 36.19±0.75*	-14.24
59235.68		-68.23±1.29, 27.45±0.92*	-9.16
59264.55		-133.20±0.93, 82.00±0.67	-10.98
59264.56		-140.56±0.82, 87.29±0.57	-15.60
59264.58	93.23±0.41	-146.59±0.76, 93.68±0.54	-10.64
59264.60		-150.17±0.78, 97.62±0.59	-8.63

Table 2. GLS orbit

Parameter	Value
<i>P</i> , d	1.217770 ± 0.000003
<i>t</i> ₀ , HJD d	2458808.8088 ± 0.0003
<i>K</i> _A , km s ⁻¹	122.80±0.23
<i>γ</i> _A , km s ⁻¹	-16.98 ± 0.16

4 RESULTS

In the Figure 2 we show the best fit by multiple-epochs binary model for epoch with maximal RV separation. We zoom into the wavelength range around the magnesium triplet and H α and in a 70 Å interval in the red arm, where many double lines are clearly visible. Both components are on main sequence, where the primary star ($T_{\text{eff}} = 6104$ K, $\log(g) = 3.86$ cgs, $[\text{Fe}/\text{H}] = -0.29$ dex, $V \sin i = 58$ km s⁻¹) contributes around 70% in the visible light, while the secondary star ($T_{\text{eff}} = 5980$ K, $\log(g) = 4.07$ cgs, $[\text{Fe}/\text{H}] = 0.02$ dex, $V \sin i = 50$ km s⁻¹) and contributes to the remaining 30%. Primary RVs derived in multy-epoch fit almost identical to ones estimated from individual spectra. The derived mass ratio $q = 0.87$ and systemic radial velocity $\gamma = -17.63$ km s⁻¹. Additionally we make another multy-epoch fit assuming same metallicity for both components, finding that it caused slight change in T_{eff} and $\log(g)$ with two components being metal-poor with $[\text{Fe}/\text{H}] = -0.19$ dex. We present all spectroscopic results in the Table 4. We can use q and $\Delta \log(g)$ to estimate ratio of stellar sizes $R_B/R_A = 0.73, 0.81$ for solution with different and same metallicity. The errors in the

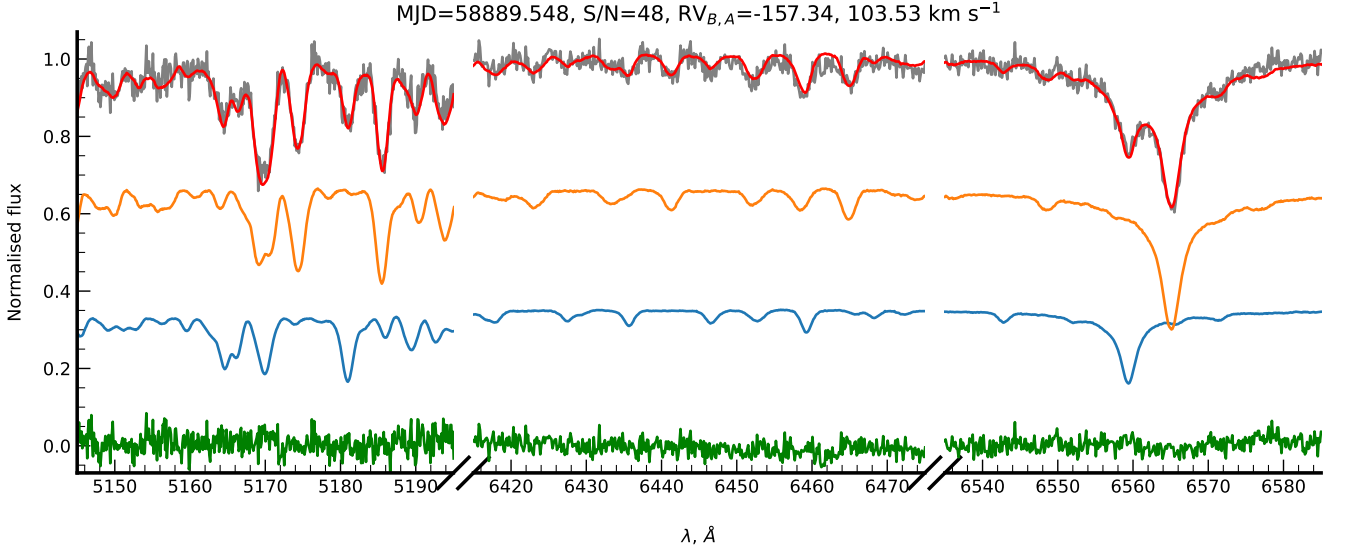


Figure 2. Example of the spectrum fitting. The observed spectrum is shown as a gray line, the best fit is shown as red line. The primary component is shown as the orange line, the secondary as a blue line. The difference O-C is shown as a green line.

spectral parameters provided by `scipy.optimize.curve_fit` are nominal and largely underestimated, so we omit them.

In Figures 3,4,5 we show best fits of the LCs (top) and RVs (bottom) by JKTEBOP. The fit residuals (O-C) are typically small (≤ 0.10 mag for ZTF r , ≤ 0.02 mag for TESS and ≤ 5 km s $^{-1}$ for RVs). Only one measurement for RV_B is off by ~ -15 km s $^{-1}$. The derived systemic velocities are very similar to the values derived from multiple-epoch spectral fit. Orbital solutions for primary star from GLS and JKTEBOP agree well taking to account uncertainties. Very small value for eccentricity ($e \leq 0.002$) confirms that orbit is circular or very close to it. The orbital solution from Table 3 in Wang et al. (2021) has $e = 1$ and $K_A = 544$ km s $^{-1}$, which is wrong due to failed optimisation. Third light contributions are significant in both TESS datasets (12 and 29 per cent) and negligible in ZTF r . This is not surprising due small aperture of TESS cameras relative to one in telescopes used for ZTF. Oblateness of the components (0.017, 0.007 for ZTF r and 0.013, 0.011 for TESS) is small (≤ 0.04), thus JKTEBOP provides reliable solution for this system (Popper & Etzel 1981). We show “corner” plots with all RP simulations in Figures C1,C2,C3, where correlations between fitted parameters can be explored. We present results from GLS and JKTEBOP in the Tables 2,3⁵

4.1 Verification with PHOEBE

We use PHOEBE (Conroy et al. 2020) to verify our results, since it allows to fit multiple LC datasets simultaneously, and updates limb darkening coefficients during the fitting. For all three LCs we convert magnitudes to fluxes and divided them by median value. We also subtract best fit t_0 from the timescale in all datasets. We use default Nelder-Mead optimiser and default “ck2004” atmospheres. Eccentricity, period and mass ratio were fixed, thus we

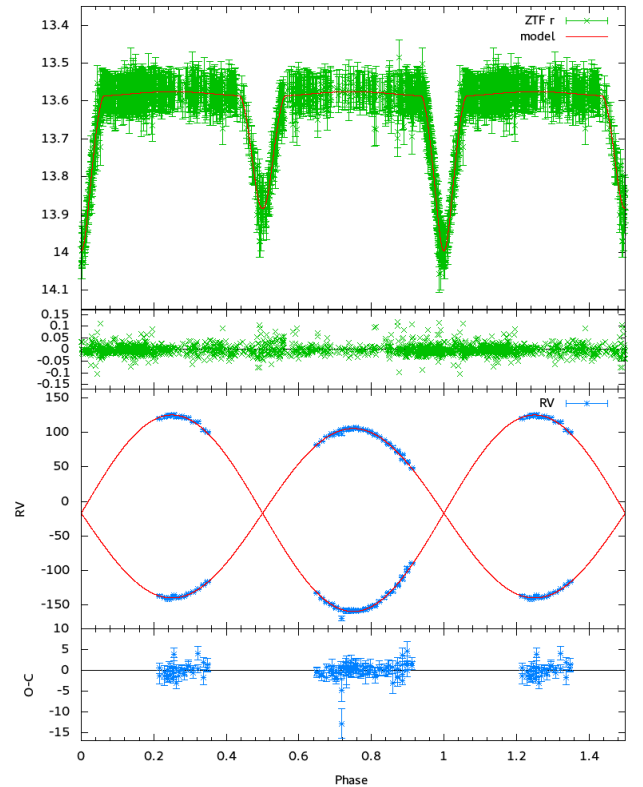


Figure 3. Phase-folded LC from ZTF r (top) and orbit (bottom) fits with JKTEBOP. In the bottom panels we show fit residuals O-C.

fit for $R_{A,B}$, $T_{\text{eff},A,B}$, γ , $a \sin i$, i and third light contribution for three LC datasets.

We present fitting results in Figures B1 and Table 5. The best fit PHOEBE model fits all three LCs well since residuals O-C are

⁵ Two additional LC datasets (ZTF g and ASAS-SN V) were also fitted, but provided poor results not consistent with ZTF r , TESS and spectroscopic fits ($R_B > R_A$), possibly due to poor coverage of eclipses.

Parameter	ZTF <i>r</i>	TESS 44	TESS 45
fixed:			
Grav. darkening _A	0.3108		0.2576
Grav. darkening _B	0.3317		0.2760
Limb darkening $c_{A,i}$	0.3029, 0.8993, -0.7099, 0.2098	0.4002, 0.4901, -0.3288, 0.0638	
Limb darkening $c_{B,i}$	0.3420, 0.7173, -0.4286, 0.0838	0.4427, 0.3238, -0.0893, -0.0390	
fitted:			
<i>J</i>	0.762±0.025	0.770±0.005	0.772±0.019
$(R_A + R_B)/a$	0.3935±0.0065	0.4063±0.0013	0.4052±0.0033
R_B/R_A	0.667±0.065	0.868±0.076	0.840±0.152
i°	83.77±1.74	81.66±0.29	81.13±0.74
$e \cos \omega$	0.0015±0.0009	0.0000±0.0001	0.0003±0.0003
$e \sin \omega$	-0.0018±0.0019	-0.0014±0.0019	-0.0021±0.0021
reflected light _A , mag	0.010±0.005	-0.003±0.001	0.005±0.002
reflected light _B , mag	0.010±0.005	0.003±0.001	0.010±0.002
L_3 , per cent	4.33 ± 9.87	12.04 ± 1.95	29.49 ± 3.93
S_0 , mag	13.586 ± 0.006	-0.009 ± 0.002	-5.546 ± 0.002
P_d	1.217783±0.000001	1.217785±0.000002	1.217785±0.000002
t_0 , HJD d	2458808.805418±0.000334	2458808.805166±0.000972	2458808.805001±0.000977
K_A , km s ⁻¹	122.95±0.21	122.99±0.20	122.99±0.25
K_B , km s ⁻¹	142.39±0.33	142.44±0.35	142.44±0.34
γ_A , km s ⁻¹	-17.15±0.13	-17.04±0.11	-17.06±0.13
γ_B , km s ⁻¹	-17.46±0.24	-17.59±0.22	-17.57±0.22
derived			
L_B/L_A	0.333±0.075	0.576±0.107	0.540±0.223
e	0.002±0.001	0.001±0.001	0.002±0.001
ω°	309.67±123.88	266.45±86.00	278.73±90.11
a , R_\odot	6.425±0.022	6.457±0.010	6.466±0.016
q	0.863±0.003	0.863±0.003	0.863±0.003
M_A , M_\odot	1.288±0.014	1.307±0.007	1.313±0.010
M_B , M_\odot	1.112±0.011	1.129±0.005	1.133±0.008
R_A , R_\odot	1.516±0.043	1.405±0.052	1.424±0.102
R_B , R_\odot	1.012±0.077	1.219±0.060	1.196±0.123
log (g) _A , cgs	4.186±0.025	4.259±0.033	4.249±0.065
log (g) _B , cgs	4.474±0.057	4.319±0.042	4.337±0.086

Table 3. JKTEBOP solutions**Table 4.** Spectral parameters.

Parameter	Star A	Star B
multi-epochs fit with free [Fe/H]		
γ , km s ⁻¹	-17.61 ± 0.28	
q_{dyn}	0.87	
T_{eff} , K	6104	5980
log (g), cgs	3.86	4.07
[Fe/H], dex	-0.29	0.02
$V \sin i$, km s ⁻¹	58	50
multi-epochs fit, assuming same [Fe/H]		
γ , km s ⁻¹	-17.54 ± 0.28	
q_{dyn}	0.87	
T_{eff} , K	6177	5820
log (g), cgs	3.88	4.00
[Fe/H], dex	-0.19	
$V \sin i$, km s ⁻¹	59	50
single-star fits of separated spectra		
T_{eff} , K	6384	6583
log (g), cgs (fixed)	4.26	4.32
[Fe/H], dex	0.02	-0.22
$V \sin i$, km s ⁻¹	58	51

insignificant. All parameters agree with JKTEBOP values for TESS datasets, therefore our usage of fixed limb darkening coefficients is reasonable. The best fit $T_{\text{eff}B}$ of the secondary agrees with spectroscopic estimate, but $T_{\text{eff}A}$ is 250 K higher. Computed $V \sin i$ are in excellent agreement with spectroscopic values. We don't use any sampling techniques to estimate errors as PHOEBE calculations are very computationally expensive in comparison with JKTEBOP.

4.1.1 RV during eclipses

By phase-folding the whole RV dataset we find that several spectra were taken exactly during eclipses. In Figure 6 we show RVs measured from these spectra together with the flux-weighted RV curves computed by PHOEBE using the best parameters. We can see that RM effect is not very strong, but it can be barely seen in our RVs data for primary eclipse.

4.2 Spectral separation.

We used “shift and add” algorithm described in [González & Levato \(2006\)](#) to extract rest-frame spectra for both components. We selected 24 spectra with $S/N \geq 40$ and $\Delta RV > 180 \text{ km s}^{-1}$. All these spectra were previously normalised during binary model fitting as described in Section 3.1.1. Radial velocities were computed using

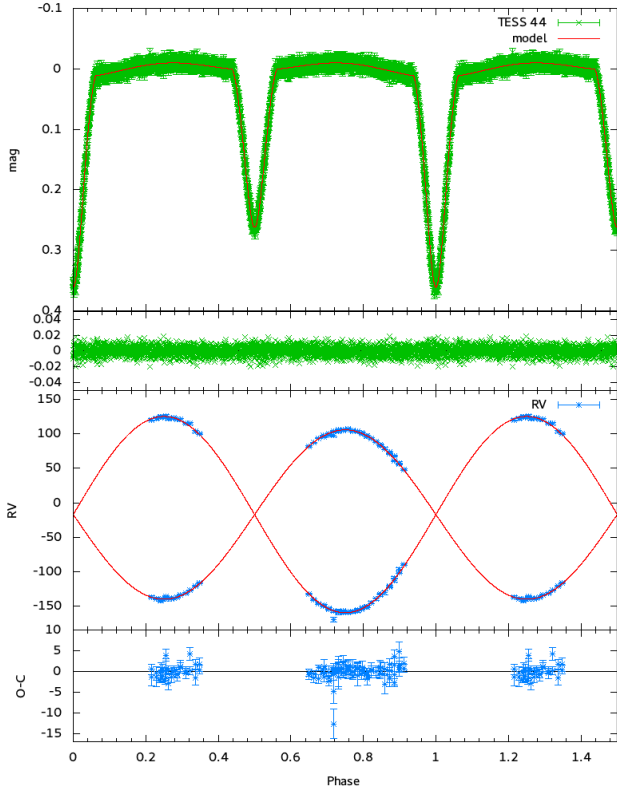


Figure 4. Phase-folded LC from TESS44 (top) and orbit (bottom) fits with JKTEBOP. In the bottom panels we show fit residuals O-C. The magnitudes are not calibrated.

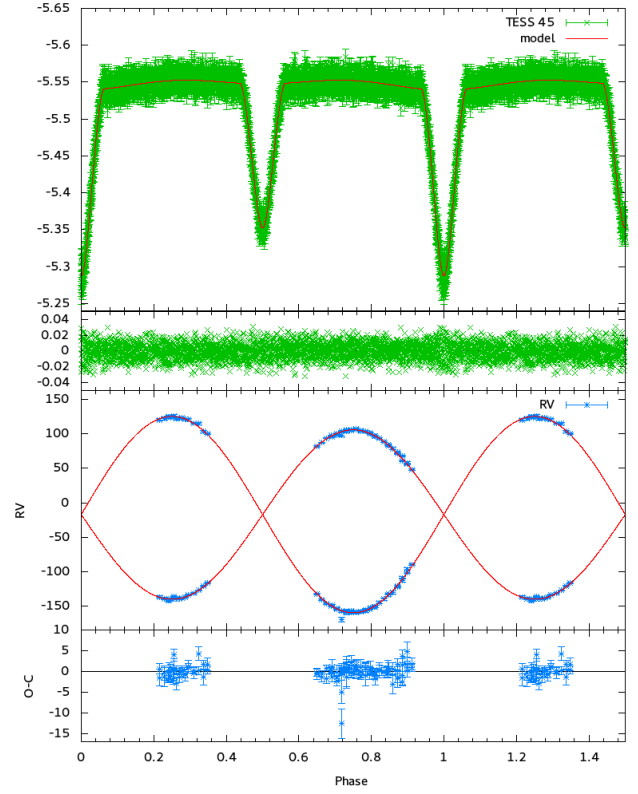


Figure 5. Phase-folded LC from TESS45 (top) and orbit (bottom) fits with JKTEBOP. In the bottom panels we show fit residuals O-C. The magnitudes are not calibrated.

Table 5. Parameters derived by PHOEBE.

Parameter	Star A	Star B
fixed		
q	0.87	
P d	1.21778	
e	0.00	
fitted		
γ , km s^{-1}	-17.25	
i°	81.63	
$a \sin i$, R_\odot	6.421	
R , R_\odot	1.427	1.219
T_{eff} , K	6414	5873
L_3 ZTF r, per cent		0.0
L_3 TESS 44, per cent		12.0
L_3 TESS 45, per cent		30.4
derived		
M , M_\odot	1.323	1.151
$\log(g)$, cgs	4.251	4.327
$V \sin i$, km s^{-1}	58.67	50.10

orbital solution. The seven iterations were enough to clearly reveal both spectral components, except for the spectral edges, where solutions start to oscillate around baseline.

These separated spectra can be fitted by single-star spectral model. We fixed $\log(g)$ to values derived based on TESS 44 LC fit, as broad spectral features were poorly recovered in resulted spectra

(González & Levato 2006). Additionally we fitted for four normalisation coefficients for each spectral arm and residual Doppler shift. Spectral errors were assigned to values corresponding to $S/N = 100$ for primary and $S/N = 80$ secondary. Regions at the spectral edges ($\lambda > 6770 \text{ \AA}$ and $\lambda < 5000 \text{ \AA}$) and 40 \AA around $H\alpha$ were assigned infinite errors. We show resulting best fits in Figure 7. Residual Doppler shifts were negligible $\Delta RV \leq 0.4 \text{ km s}^{-1}$, as expected. For primary component we got $T_{\text{eff}A} = 6384 \text{ K}$, $[\text{Fe}/\text{H}]_A = 0.02 \text{ dex}$ and $V \sin i_A = 58 \text{ km s}^{-1}$ which is similar to results from multiple-epochs fit. Even masked $H\alpha$ region is modelled well. However we were unable to find good solution for secondary component which is consistent with results from multiple-epochs fit. We got much higher temperature $T_{\text{eff}B} = 6583 \text{ K}$, probably due to masked $H\alpha$ line wings, although $[\text{Fe}/\text{H}] = -0.22 \text{ dex}$ and $V \sin i = 51 \text{ km s}^{-1}$ were similar to results from multiple-epochs fit. We tried to fit these spectra again with $H\alpha$ region and found $T_{\text{eff}A,B} = 6407, 5920 \text{ K}$, $[\text{Fe}/\text{H}] = 0.05, -0.81 \text{ dex}$ and $V \sin i = 57, 51 \text{ km s}^{-1}$. This solution for secondary have acceptable temperature, but its metallicity is very small. Note that $V \sin i$ almost unchanged, therefore our spectroscopic analysis can provide stable recovery of this parameter.

Spectral separation results are less reliable in comparison with multiple-epochs fits, since they have lost information on relative contribution of the components and broad spectral features. We therefore don't use them in further analysis.

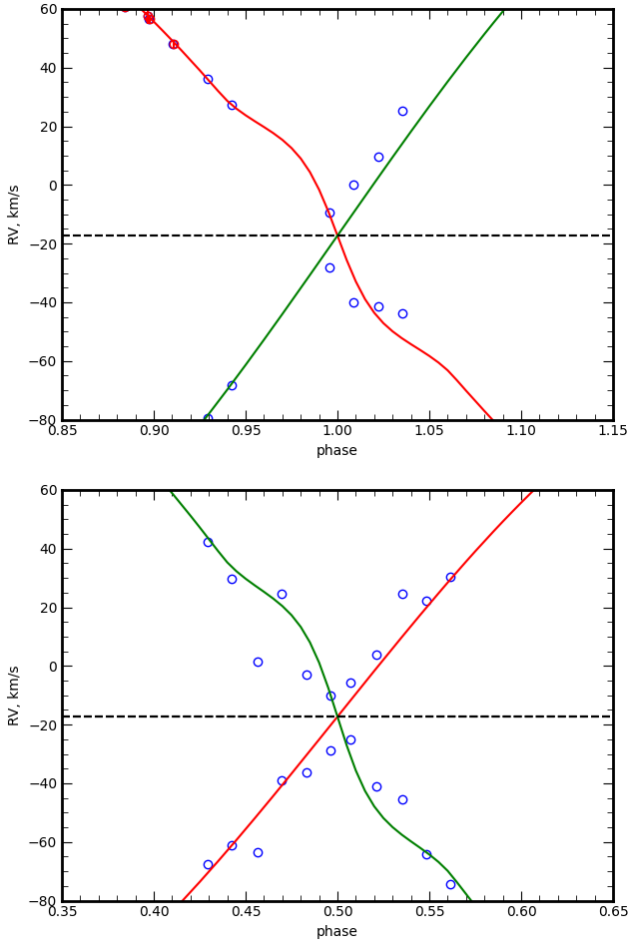


Figure 6. Radial velocities measured during eclipses together with best fit PHOEBE model for primary (red line) and secondary (green line) components. Blue datapoints were not used in the fit.

5 DISCUSSION

5.1 System parameters

Physical parameters of the components suggests that system consists two fast rotating stars, which are heavier and larger than Sun. They form close system with circular orbit, slightly inclined to the line of sight, therefore we have Algol type variable, with partial eclipses. Both components are on the main sequence, mass transfer is not started yet, as both components are smaller than their Roche lobes. The spectroscopic solution computed with assumption of the same $[\text{Fe}/\text{H}]$ for both components have $R_B/R_A = 0.81$ which is very close to the value $R_B/R_A = 0.868 \pm 0.076$ from the TESS 44 LC fit. Relatively large projected rotational velocities measured from the spectra are in perfect agreement with $V \sin i_{\text{sync } A,B} = 57.8 \pm 2.0, 50.0 \pm 2.5 \text{ km s}^{-1}$ computed using TESS LC fit parameters, suggesting spin-orbit synchronisation.

Surface gravities derived by JKTEBOP are significantly larger than spectroscopic ones. There is a bias of $\Delta \log(g) = 0.3 - 0.4$ dex, which is larger than expected $\log(g)$ uncertainties given in Section 3.1.3. Similar bias was observed in Kovalev et al. (2019) for open cluster NGC 2243, where stars near the turn-off have spectroscopic $\log(g)$ smaller than $\log(g)$ from the PARSEC isochrone (Marigo et al. 2017). Thus such bias can be related to inaccuracy of

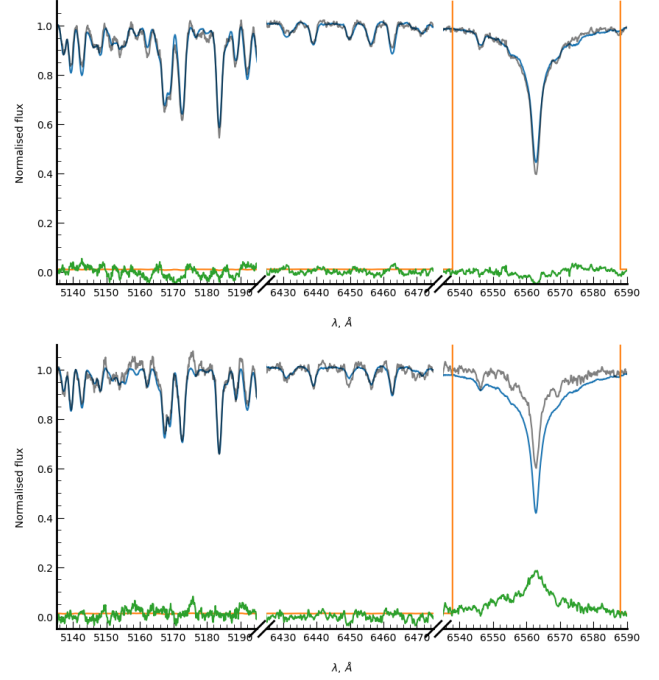


Figure 7. Separated spectra fitted by the single-star spectral model. The observed spectrum is shown as a gray line, the best fit is shown as blue line. The orange line is an error spectrum and the difference O-C is shown as a green line. The primary component is shown on the top panel, the secondary is shown on the bottom panel.

Parameter	Value	reference
P , d	1.2177044	ZTF
P , d	1.217726	ASAS-SN
d , pc	1080 ¹³²⁰	GDR3 MSC
A_G , mag	0.3131 ^{0.9389}	GDR3 MSC
$[\text{Fe}/\text{H}]$, dex	0.13 ^{0.5}	GDR3 MSC
$T_{\text{eff } A,B}$, K	6127 ⁷⁸²¹ , 5885 ⁶⁵⁵⁸	GDR3 MSC
$\log(g)_{A,B}$, cgs	4.28 ^{4.52} , 4.57 ^{5.2}	GDR3 MSC
$T_{\text{eff } A,B}$, K	6193 \pm 39, 5654 \pm 57	Xiong
$\log(g)_{A,B}$, cgs	4.09 \pm 0.08, 4.64	Xiong
$[\text{Fe}/\text{H}]_{A,B}$, dex	-0.250 \pm 0.110	Xiong
$M_{A,B}$, M_{\odot}	1.407 \pm 0.011, 1.214 \pm 0.011	Xiong
$R_{A,B}$, R_{\odot}	1.501 \pm 0.050, 0.868 \pm 0.027	Xiong
$V \sin i_A$, km s^{-1}	91.80	Xiong
q	0.862 \pm 0.015	Xiong
age t, Gyr	5.664 ^{6.317}	GDR3 FLAME*
age log t, yr	9.572 \pm 0.246	UNIDAM*

Table 6. Literature data compilation from ZTF Chen et al. (2020), ASAS-SN Jayasinghe et al. (2018), Gaia DR3 FLAME and Multiple Star Classifier (MSC) Gaia Collaboration et al. (2022), UNIDAM Mints & Hekker (2017) and Xiong et al. (submitted). Gaia DR3 values provided with 16 and 84 percentiles. (*) assuming single star.

the spectral models. Note that difference of spectroscopic surface gravities $\log(g)_B - \log(g)_A = 0.12$ is comparable to difference $(\log(g)_B - \log(g)_A = 0.06)$ from the TESS LC fit, because we use it to scale relative contribution of the components in the spectrum.

We explore previously reported measurement for this system and collect them in Table 6. Orbital periods from ZTF and ASAS-

SN V are in good agreement with our estimations, although they are slightly shorter. Recent Gaia DR3 presents very interesting estimates by Multiple Star Classifier (MSC) [Gaia Collaboration et al. \(2022\)](#), where they tried to model observed low resolution *BP*, *RP* spectra using two stellar components. These estimates agree very well with our T_{eff} from multiple-spectra fit and $\log(g)$ from TESS 44 dataset, although our $[\text{Fe}/\text{H}]$ is 0.3 dex smaller. This is well-behaved solution based on goodness-of-fit score $\text{logposterior_msc}=495^6$. We also retrieve all their 100 Monte Carlo samples and plot them in Figure D1.

Xiong et al. (submitted) also used LAMOST MRS, ZTF, ASAS-SN data to analyse this system with PHOEBE. For primary star in the system they got M_A and R_A larger than our estimates, but their $T_{\text{eff}A}$ agrees with our value. For the secondary star their M_B is higher, but R_B and $T_{\text{eff}B}$ are significantly smaller than our estimates. Their $[\text{Fe}/\text{H}]$ for the system is slightly smaller than our estimate. We think that disagreement is due to their usage of less precise LC datasets and usage of spectral parameters from the second minimum for initialisation. Likely they underestimated orbital inclination, which led to much larger masses.

We take parameters from TESS 44 fit by JKTEBOP together with T_{eff} and $[\text{Fe}/\text{H}]$ from multiple-spectra fit, assuming same $[\text{Fe}/\text{H}]$ as a final solution.

5.2 Age determination

We use the grid of PARSEC isochrones ([Marigo et al. 2017](#)), computed at metallicity $[\text{Fe}/\text{H}] = -0.19$ dex, together with masses and radii from all RP simulations for TESS 44 dataset to derive system's age, assuming that two stars evolve separately, but have the same age. All fitted age solutions have median $\log t = 9.195^{9.230}_{9.175}$ yr (1.56 Gyr) with 16 and 84 percentiles, which is significantly younger than Sun. This is very different from the single star age values $t = 5.664^{6.317}_{4.983}$ Gyr from GDR3 FLAME ([Gaia Collaboration et al. 2022](#)) and $\log t = 9.572 \pm 0.246$ (3.73 Gyr) from ([Mints & Hekker 2017](#)). The theoretical circularisation time for orbit with given q and P , using Formula 6.2 from [Zahn \(1977\)](#): $\log t_{\text{circ}} = 9.47$ yr (2.95 Gyr) is larger than our estimate of the system's age, therefore tidal friction was very efficient, possibly was also accompanied by strong magnetic interactions.

However we should note, that theoretical models have difficulty to describe this system. In Figure 8 we plot grid of PARSEC isochrones computed for $[\text{Fe}/\text{H}] = -0.6, -0.2, 0.2$ dex and five ages in range from 1 to 5 Gyr. Our best fit isochrone is also shown, together with our best estimates and parameters from Xiong et al. (submitted). Generally theoretical models are steeper in the mass-radius plane than our estimates, therefore best-fit isochrone goes through upper errorbar for the primary and lower errorbar for the secondary. Similar discrepancy was found by [Southworth et al. \(2011\)](#) for XY Ceti. In the lower panel with the mass- T_{eff} plane, you can see that theoretical values of T_{eff} are significantly larger than our T_{eff} estimates at corresponding masses. Only isochrones with significant super-solar metallicity will be able to match them. Therefore our results suggest that PARSEC isochrones are unable to model this close dEB system properly and our estimate of age is not reliable.

Recently [del Burgo & Allende Prieto \(2018\)](#) employed a set

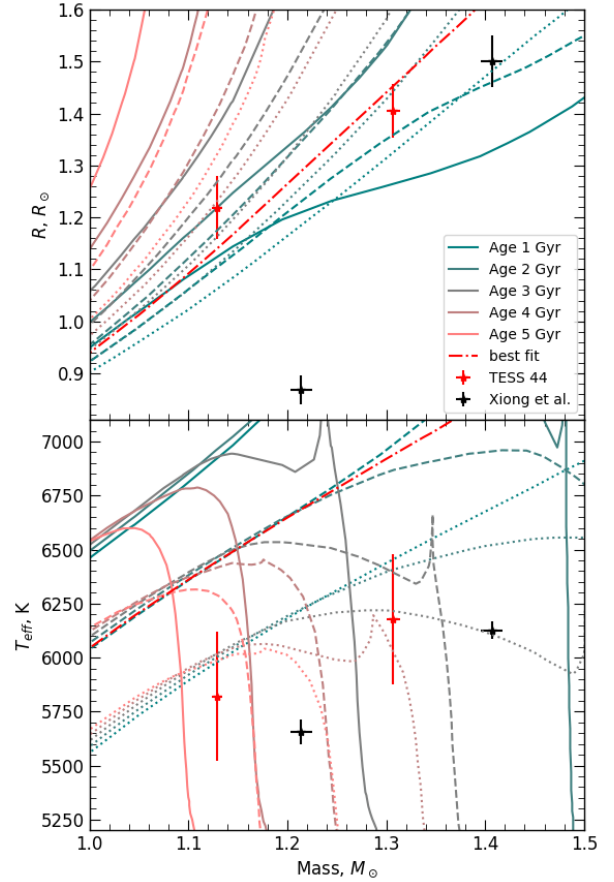


Figure 8. The grid of PARSEC isochrones computed for $[\text{Fe}/\text{H}] = -0.6$ (solid lines), -0.2 (dashed lines), 0.2 dex (dotted lines) and five ages in range from 1 to 5 Gyr. Our best fit ($[\text{Fe}/\text{H}] = -0.19$ dex, age 1.57 Gyr) isochrone is also shown (red dot-dashed line), together with our best estimates and primary parameters from Xiong et al. submitted.

of well studied dEBs to test PARSEC isochrones, using Bayesian framework to infer masses, distances and ages, taking radii, T_{eff} and $[\text{Fe}/\text{H}]$ as input. They found that PARSEC models systematically underestimate masses, although discrepancies are not so important for main sequence. For example for close dEB system UZ Dra with similar parameters to J064726.39+223431.6 ($P = 3.261$ d, $R_{A,B} = 1.31 \pm 0.03, 1.15 \pm 0.02 R_{\odot}$, $T_{\text{eff}A,B} = 6209 \pm 114, 5984 \pm 110$ K, $M_{A,B} = 1.34 \pm 0.02, 1.23 \pm 0.02 M_{\odot}$, no estimate of $[\text{Fe}/\text{H}]$ yet) they inferred $M_{A,B}^{\text{fit}} = 1.13 \pm 0.09, 1.04 \pm 0.09 M_{\odot}$, assuming solar metallicity for this system.

Additionally we check another two sets of theoretical models by [Dotter \(2016\)](#) and [Claret \(2019\)](#), but find no improvement relative to PARSEC.

6 CONCLUSIONS

We present a study of dEB SB2 J064726.39+223431.6 system using spectra from the LAMOST-MRS survey and photometrical data. We use full-spectrum fitting to derive radial velocities and spectral parameters. The orbital solution and light curves from ZTF and TESS suggests, that it is a close pair on circular orbit. We have measured the masses of the stars to accuracies of 1 per cent and the radii to accuracies of 5 per cent. System shows strong evidence for spin-

⁶ https://gea.esac.esa.int/archive/documentation/GDR3/Data_analysis/chap_cu8par/sec_cu8par_apsis/ssc_cu8par_apsis_msc.html

orbit synchronisation. We find discrepancy between spectroscopic $\log(g)$ and $\log(g)$ calculated using parameters from LC fitting. Theoretical isochrones also unable to model measured mass- T_{eff} relations at derived metallicity. Derived age of the system indicates that both components are still on the main sequence.

ACKNOWLEDGEMENTS

MK is grateful to his parents, Yuri Kovalev and Yulia Kovaleva, for their full support in making this research possible. The work is supported by the Natural Science Foundation of China (Nos. 11733008, 12090040, 12090043, 11521303, 12125303). Guoshoujing Telescope (the Large Sky Area Multi-Object Fiber Spectroscopic Telescope LAMOST) is a National Major Scientific Project built by the Chinese Academy of Sciences. Funding for the project has been provided by the National Development and Reform Commission. LAMOST is operated and managed by the National Astronomical Observatories, Chinese Academy of Sciences. The authors gratefully acknowledge the “PHOENIX Supercomputing Platform” jointly operated by the Binary Population Synthesis Group and the Stellar Astrophysics Group at Yunnan Observatories, Chinese Academy of Sciences. This research has made use of NASA’s Astrophysics Data System, the SIMBAD data base, and the VizieR catalogue access tool, operated at CDS, Strasbourg, France. It also made use of TOPCAT, an interactive graphical viewer and editor for tabular data (Taylor 2005). Funding for the TESS mission is provided by NASA’s Science Mission directorate. This paper includes data collected by the TESS mission, which is publicly available from the Mikulski Archive for Space Telescopes (MAST). This work has made use of data from the European Space Agency (ESA) mission *Gaia* (<https://www.cosmos.esa.int/gaia>), processed by the *Gaia* Data Processing and Analysis Consortium (DPAC, <https://www.cosmos.esa.int/web/gaia/dpac/consortium>). Funding for the DPAC has been provided by national institutions, in particular the institutions participating in the *Gaia* Multilateral Agreement.

Based on observations obtained with the Samuel Oschin Telescope 48-inch and the 60-inch Telescope at the Palomar Observatory as part of the Zwicky Transient Facility project. ZTF is supported by the National Science Foundation under Grant No. AST-2034437 and a collaboration including Caltech, IPAC, the Weizmann Institute for Science, the Oskar Klein Center at Stockholm University, the University of Maryland, Deutsches Elektronen-Synchrotron and Humboldt University, the TANGO Consortium of Taiwan, the University of Wisconsin at Milwaukee, Trinity College Dublin, Lawrence Livermore National Laboratory, and IN2P3, France. Operations are conducted by COO, IPAC, and UW. This research has made use of the NASA/IPAC Infrared Science Archive, which is funded by the National Aeronautics and Space Administration and operated by the California Institute of Technology.

DATA AVAILABILITY

The data underlying this article will be shared on reasonable request to the corresponding author.

REFERENCES

Brasseur C. E., Phillip C., Fleming S. W., Mullally S. E., White R. L., 2019, *Astrotcut: Tools for creating cutouts of TESS images*, *Astrophysics Source Code Library*, record ascl:1905.007 (ascl:1905.007)

- Chen X., Wang S., Deng L., de Grijs R., Yang M., Tian H., 2020, *ApJS*, **249**, 18
- Claret A., 2017, *A&A*, **600**, A30
- Claret A., 2019, *A&A*, **628**, A29
- Claret A., Bloemen S., 2011, *A&A*, **529**, A75
- Conroy K. E., et al., 2020, *ApJS*, **250**, 34
- Cui X.-Q., et al., 2012, *Research in Astronomy and Astrophysics*, **12**, 1197
- Czesla S., Schröter S., Schneider C. P., Huber K. F., Pfeifer F., Andreasen D. T., Zechmeister M., 2019, *PyA: Python astronomy-related packages* (ascl:1906.010)
- Dotter A., 2016, *ApJS*, **222**, 8
- El-Badry K., et al., 2018, *MNRAS*, **476**, 528
- Feinstein A. D., et al., 2019, *PASP*, **131**, 094502
- Foreman-Mackey D., 2016, *The Journal of Open Source Software*, **1**, 24
- Gaia Collaboration et al., 2022, arXiv e-prints, p. arXiv:2208.00211
- González J. F., Levato H., 2006, *A&A*, **448**, 283
- Grupp F., 2004a, *A&A*, **420**, 289
- Grupp F., 2004b, *A&A*, **426**, 309
- Jayasinghe T., et al., 2018, *MNRAS*, **477**, 3145
- Kovalev M., 2019, PhD thesis, IMPRS-HD, doi:10.11588/heidok.00027411
- Kovalev M., 2022, arXiv e-prints, p. arXiv:2207.06996
- Kovalev M., Bergemann M., Ting Y.-S., Rix H.-W., 2019, *A&A*, **628**, A54
- Kovalev M., Li Z., Zhang X., Li J., Chen X., Han Z., 2022, *MNRAS*, **513**, 4295
- Liu C., et al., 2020, arXiv e-prints, p. arXiv:2005.07210
- Marigo P., et al., 2017, *ApJ*, **835**, 77
- McLaughlin D. B., 1924, *ApJ*, **60**, 22
- Mints A., Hekker S., 2017, *A&A*, **604**, A108
- Popper D. M., Etzel P. B., 1981, *AJ*, **86**, 102
- Ricker G. R., et al., 2015, *Journal of Astronomical Telescopes, Instruments, and Systems*, **1**, 014003
- Rossiter R. A., 1924, *ApJ*, **60**, 15
- Southworth J., 2013, *A&A*, **557**, A119
- Southworth J., Pavlovski K., Tamajo E., Smalley B., West R. G., Anderson D. R., 2011, *MNRAS*, **414**, 3740
- Stassun K. G., et al., 2019, *AJ*, **158**, 138
- Taylor M. B., 2005, in Shopbell P., Britton M., Ebert R., eds, *Astronomical Society of the Pacific Conference Series Vol. 347, Astronomical Data Analysis Software and Systems XIV*, p. 29
- Ting Y.-S., Conroy C., Rix H.-W., Cargile P., 2019, *ApJ*, **879**, 69
- Torres G., 2021, *Research Notes of the American Astronomical Society*, **5**, 256
- Wang S., et al., 2021, *Research in Astronomy and Astrophysics*, **21**, 292
- Watson C. L., Henden A. A., Price A., 2006, *Society for Astronomical Sciences Annual Symposium*, **25**, 47
- Zahn J. P., 1977, *A&A*, **57**, 383
- Zechmeister M., Kürster M., 2009, *A&A*, **496**, 577
- Zhao G., Zhao Y.-H., Chu Y.-Q., Jing Y.-P., Deng L.-C., 2012, *Research in Astronomy and Astrophysics*, **12**, 723
- del Burgo C., Allende Prieto C., 2018, *MNRAS*, **479**, 1953

APPENDIX A: SPECTRAL MODELS

The synthetic spectra are generated using NLTE MPiA online-interface <https://nlte.mpia.de> (see Chapter 4 in Kovalev 2019) on wavelength intervals 4870:5430 Å for the blue arm and 6200:6900 Å for the red arm with spectral resolution $R = 7500$. We use NLTE (non-local thermodynamic equilibrium) spectral synthesis for H, Mg I, Si I, Ca I, Ti I, Fe I and Fe II lines (see Chapter 4 in Kovalev 2019, for references).

The grid of models (6200 in total) is computed for points randomly selected in a range of T_{eff} between 4600 and 8800 K, $\log(g)$ between 1.0 and 4.8 (cgs units), $V \sin i$ from 1 to 300 km s⁻¹ and

[Fe/H]⁷ between -0.9 and $+0.9$ dex. The model is computed only if linear interpolation of MAFAGS-OS (Grupp 2004a,b) stellar atmosphere is possible for a given point in parameter space. Micro-turbulence is fixed to $V_{\text{mic}} = 2 \text{ km s}^{-1}$ for all models. The grid is randomly split on training (70%) and cross-validation (30%) sets of spectra, which are used to train *The Payne* spectral model (Ting et al. 2019). The neural network (NN) consists of two layers of 300 neurons each with rectilinear unit (ReLU)⁸ activation functions. We train separate NNs for each spectral arm. The median approximation error is less than 1% for both arms. We use output of *The Payne* as single-star spectral model.

APPENDIX B: PHOEBE BEST FIT SOLUTION

We show best fit LC solution obtained with PHOEBE in Figure B1.

APPENDIX C: RESIDUAL-PERMUTATION SIMULATIONS

In Figures C1, C2, C3 we show corner plots (Foreman-Mackey 2016) with all residual-permutation simulation results for J , R_B/R_A , i , L_B/L_A , and $\log(g)_{A,B}$ for ZTF r and TESS LCs. There is strong correlation between J and R_B/R_A clearly visible for all datasets, which can propagate into other parameters like L and $\log(g)$. However the most precise TESS 44 dataset is less affected.

APPENDIX D: GAIA DR3 MONTE CARLO MULTIPLE STAR CLASSIFIER SAMPLE

In Figure D1 we show corner plot (Foreman-Mackey 2016) with Monte Carlo Multiple Star Classifier sample from Gaia Collaboration et al. (2022). We select subsample with $A_0 > 0.2$ mag (70 datapoints). These results have higher \log_{post} . We compute 16, 50 and 84 percentiles for them and median values are comparable to out final parameters, however metallicity and $\log(g)_B$ are higher. The remaining 30 datapoints have smaller \log_{post} and have $\log(g)_{A,B} \sim 4.7$ cgs. This is probably solutions from local maximum of the posterior.

This paper has been typeset from a \LaTeX file prepared by the author.

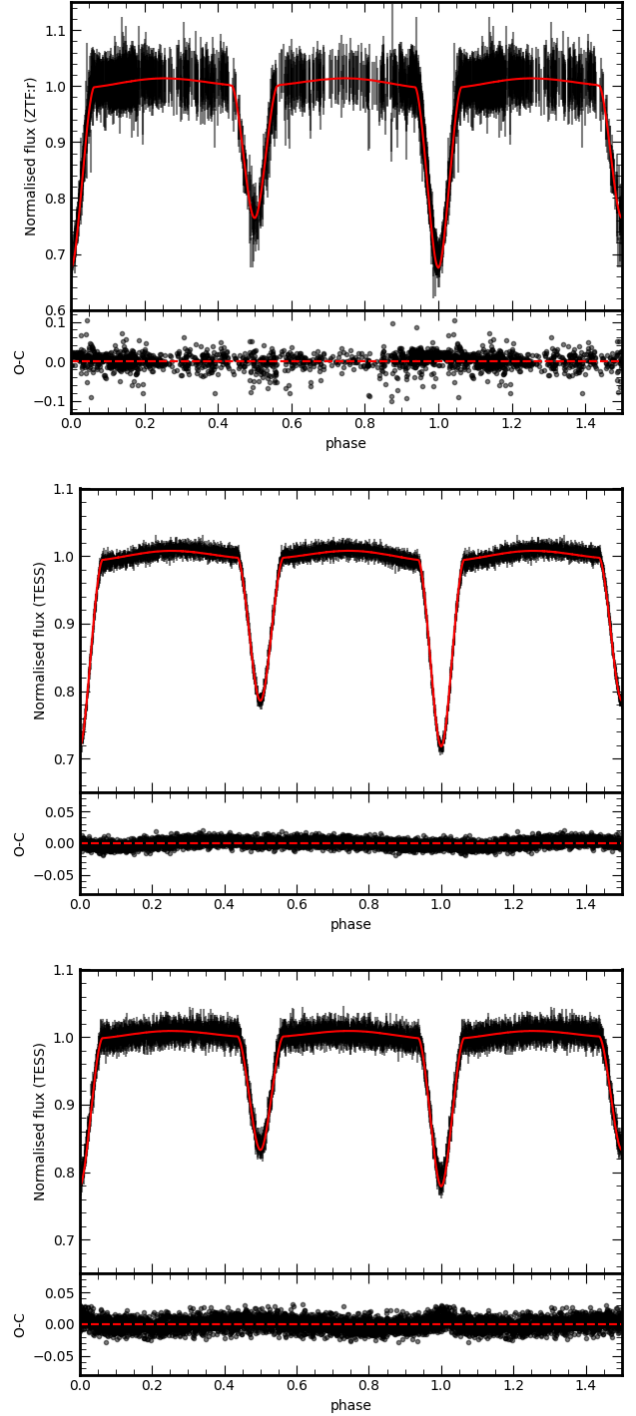


Figure B1. The best fit PHOEBE model for ZTF r (top), TESS 44 (middle) and TESS 45 (bottom) LCs.

⁷ We used [Fe/H] as a proxy of overall metallicity, abundances for all elements are scaled with Fe.

⁸ $\text{ReLU}(x) = \max(x, 0)$

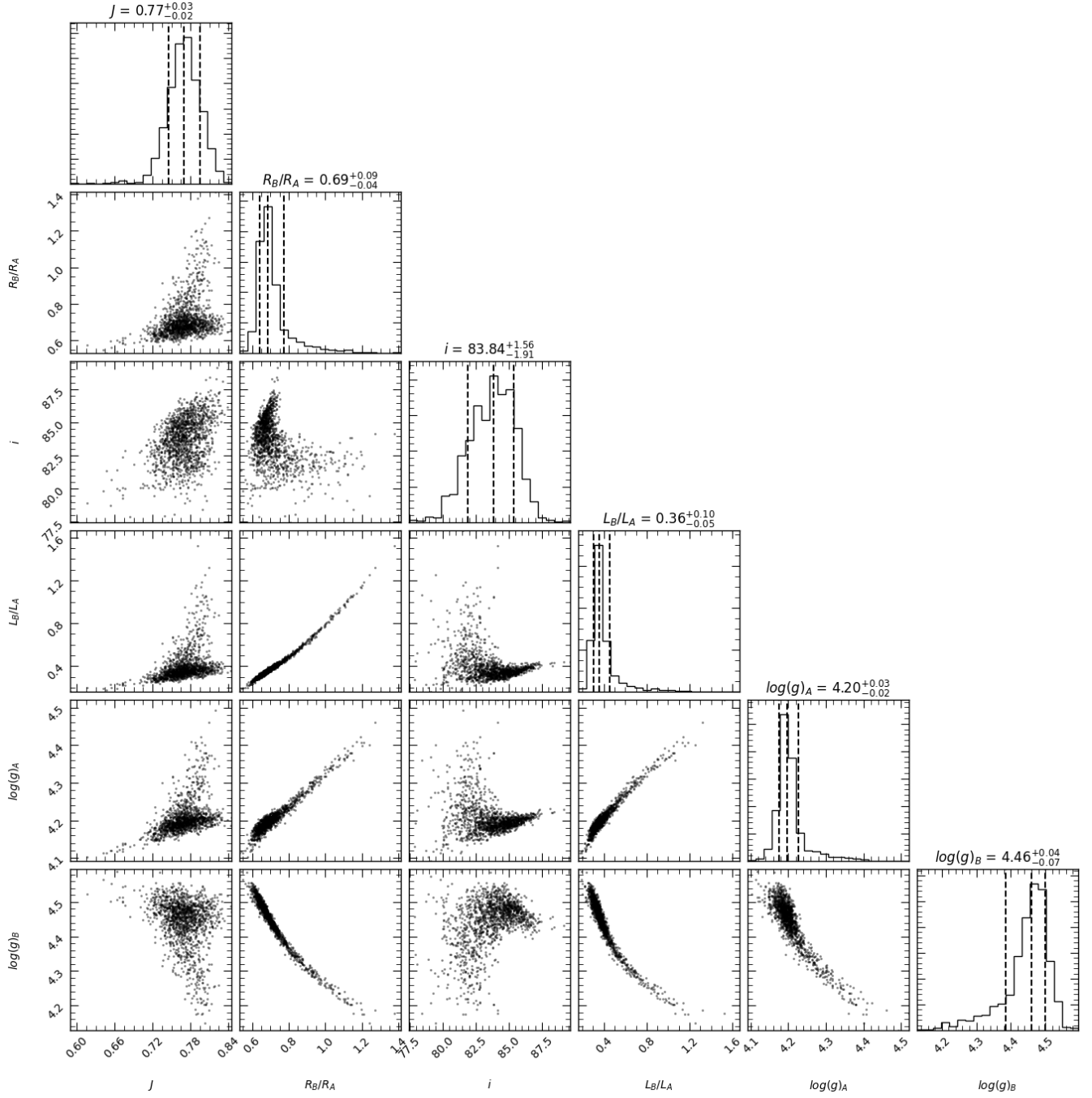


Figure C1. Corner plot for the residual-permutation simulations of ZTF r solution. Titles show 16, 50 and 84 percentiles.

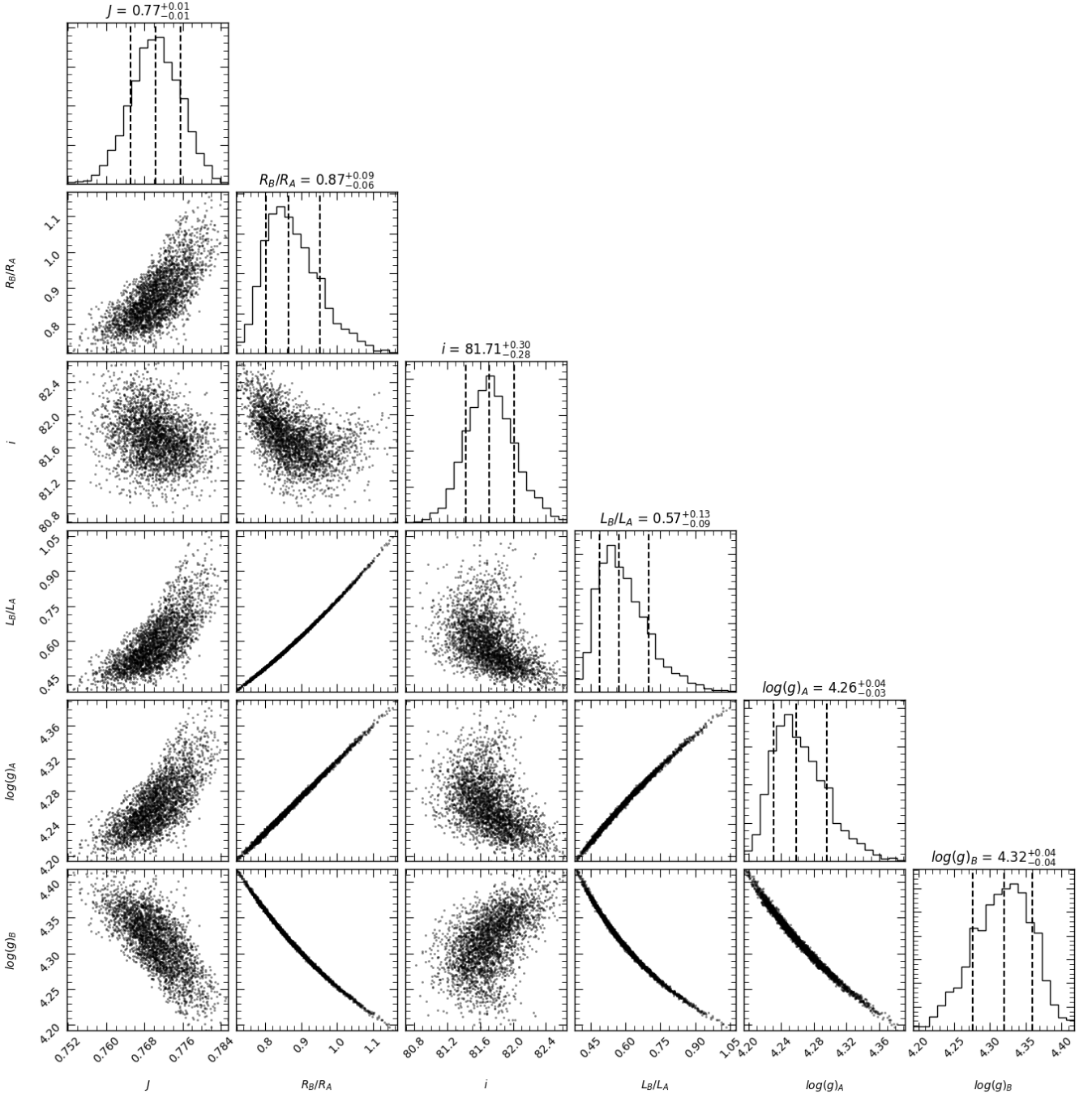


Figure C2. Corner plot for the residual-permutation simulations of TESS 44 solution. Titles show 16, 50 and 84 percentiles.

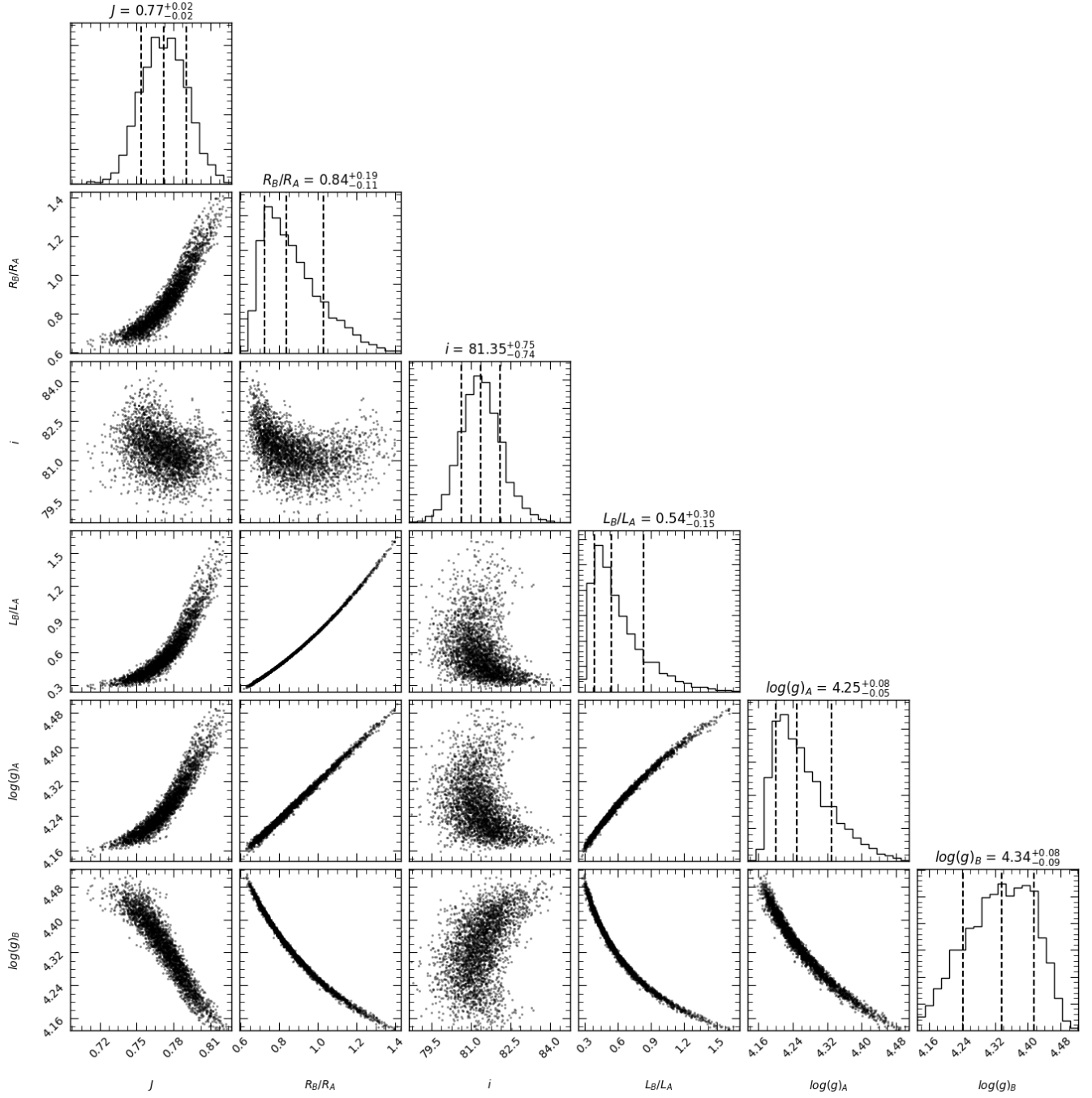


Figure C3. Corner plot for the residual-permutation simulations of TESS 45 solution. Titles show 16, 50 and 84 percentiles.

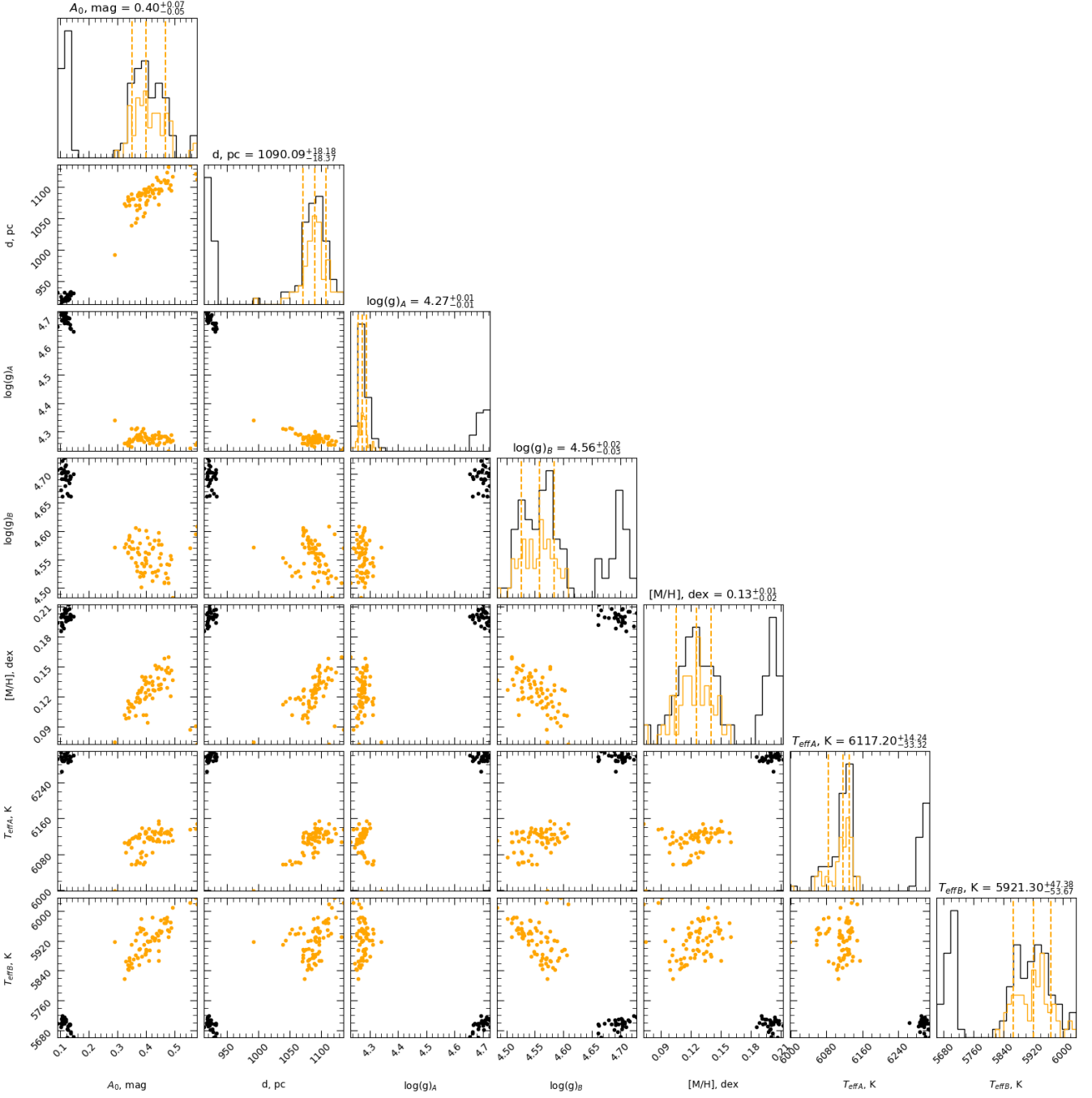


Figure D1. Corner plot for Gaia DR3 Multiple Star Classifier sample. Titles show 16, 50 and 84 percentiles for subsample with $A_0 > 0.2$ mag.